



# Electrochemical energy storage performance of asymmetric PEDOT and graphene electrode-based supercapacitors using ionic liquid gel electrolyte

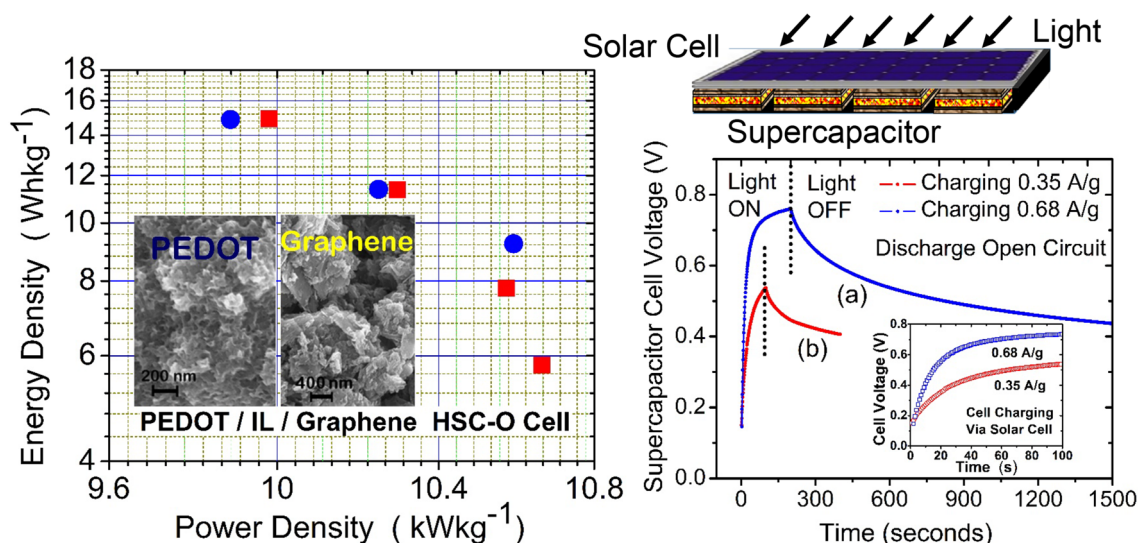
Amr M. Obeidat<sup>1,2</sup> · A. C. Rastogi<sup>1</sup>

Received: 6 October 2017 / Accepted: 5 March 2018 / Published online: 10 March 2018  
© Springer Science+Business Media B.V., part of Springer Nature 2018

## Abstract

Electrochemical and energy storage properties of thin layer hybrid supercapacitors in the solid-state platform utilizing two asymmetric poly(3,4-ethylenedioxythiophene) PEDOT and graphene electrodes with 1-butyl-3-methylimidazolium tetrafluoroborate ([BMIM][BF<sub>4</sub>]) ionic liquid gel electrolyte are described. In hybrid design, energy storage is by electrical double-layer charges at graphene and through reversible faradic redox process at PEDOT while the high operational voltage of 2.7 V due to ionic liquid electrolyte boosted the energy density. The PEDOT film was synthesized by pulsed current electropolymerization as confirmed by Raman analysis and was in the microporous form for pervasive access to electrolyte ions. Areal mass of PEDOT was varied and the hybrid supercapacitors with PEDOT/graphene active mass ratio 0.35, 0.46, and 0.78 were analyzed for specific capacity and charge–discharge behavior in order to balance the charge and charge transfer kinetics for optimized hybrid supercapacitor device. Randles–Sevcik analysis showed high ClO<sub>4</sub><sup>−</sup> ion diffusivity  $6.6 \times 10^{-9} \text{ cm}^2 \text{ s}^{-1}$  at 2.7 V in ionic liquid gel which is comparable to liquid electrolytes. By combining the micro-porosity of PEDOT, large  $600 \text{ m}^2 \text{ g}^{-1}$  surface area of graphene and high 2.7 V stability of ([BMIM][BF<sub>4</sub>]) ionic liquid gel electrolyte, energy density of  $14.9 \text{ Wh kg}^{-1}$  at specific power rating of  $9.8 \text{ kW kg}^{-1}$  are realized and stability over 2000 charge–discharge cycles is shown. Impedance and Bode analysis using equivalent circuit model is presented. The characteristics of solar electricity storage are described which can have applications as autonomous energy source harvesting light energy for powering portable power electronics.

## Graphical Abstract



**Keywords** Hybrid supercapacitor · Ionic liquid gel · Graphene · PEDOT · Energy storage · Ragone plots · Electropolymerization

## 1 Introduction

Supercapacitors in the solid-state design and flexible format offer highly adaptable energy storage solution in meeting the demands of the emergent flexible, wearable, and low cost disposable electronics [1–4]. Supercapacitors have lower specific energy compared to the battery, but with faster charge–discharge capability these can be of potential advantage for such applications. Furthermore, when combined with the ambient energy sources such as vibration using piezoelectric resonators [5] and light using solar cells [6, 7], these can harvest, store, and condition energy at high power needed for a number of electronic device functions such as those activated by internet [8] and others like wireless sensor networks [9]. For such applications, supercapacitors in solid-state configuration comprising environmentally benign materials with attributes of high energy density, long cycle life, high power delivery, and having the ability to seamlessly integrate with electronics are required.

Energy storage in supercapacitors is basically capacitive in nature utilizing the electrical double-layer (EDL) and Faradaic redox mechanisms [10]. The EDL supercapacitors are based on structured carbons, carbon nanotubes (CNT), variants of graphene, and activated carbon (AC) electrodes [11, 12], which by virtue of large surface area and distributed open pore structure highly accessible to the electrolyte ions can enhance the energy density via higher specific capacitance. The pseudocapacitors utilize the fast and reversible Faradaic surface and bulk redox reactions to achieve high specific capacitance using the transition metal (hydro) oxides [13] and electrically conducting polymers (ECP) [14] electrodes in the nanostructured forms for increased ion access and rapid redox reactions [15, 16]. In addition to the increase in specific capacitance, the increase in energy density can also be achieved in supercapacitors that operate at higher voltages based on the relation,  $E = (1/2)CV^2$ . One approach to enhance the functional voltage range is to have two asymmetric electrodes rooted in different storage mechanisms operating in different electrochemical potential ranges forming the hybrid supercapacitor [17, 18]. Asymmetric combination of metal oxides–hydroxides, Ni(OH)<sub>2</sub>, RuO<sub>2</sub>, MnO<sub>2</sub> as positive and the structured carbons, CNT and graphene as negative electrodes [19–23], or the combination of carbon electrode with conducting polymers like polyaniline (PANI), PEDOT, and polypyrrole (Ppy) have been reported [24–26]. The second approach for higher supercapacitor operating voltages is to use organic electrolytes that are stable up to ~3 V, but have associated concerns of low electrical conductivity, high flammability, toxicity,

high cost, and overcharging. For this reason, the hybrid supercapacitors described above are mostly based on aqueous electrolytes which have no such safety concerns. However, the liquid electrolyte-based supercapacitors could only be assembled in the conventional cylindrical metal-encased structures which are bulky and not adaptive to portable and flexible electronics applications.

A better alternative is the supercapacitors with solid-state electrolytes, which can be integrated with low-power electronics without any form factor concerns due to their thin flat and leak-proof assembly. Most past reports on solid-state supercapacitors are based on symmetrical electrodes using conducting polymers [27, 28], CNT–ECP composites [29, 30], graphene [31], and composites of structured carbons with metal oxides [32, 33]. The hybrid supercapacitors in the solid-state design using two dissimilar electrodes have not been much studied except for a few reports based on one electrode of conducting polymer or metal oxide (Mn<sub>3</sub>O<sub>4</sub>, RuO<sub>2</sub>, Fe<sub>2</sub>O<sub>3</sub>) and the other of carbonaceous (CNT, graphene) electrode [34–36] as well as two different conducting polymers such as PEDOT–PANI [37]. These solid-state supercapacitors are based on polymer-gel electrolyte comprising of poly vinyl alcohol (PVA) or poly(ethylene oxide) (PEO) and electrolyte (H<sub>3</sub>PO<sub>4</sub>, LiClO<sub>4</sub>, H<sub>2</sub>SO<sub>4</sub>) in ethylene carbonate (EC), dimethyl carbonate (DMC), or diethyl carbonate (DEC) organic solvents. Their major drawback is the poor electrical conductivity and aging effects that cause internal loss of capacity affecting the performance of supercapacitors. On the other hand, the ionic liquid gel electrolytes that have more preferred characteristics like, high ionic conductivity, wide (~3.0 V) potential window, air and moisture stability, and wide functional –10 to 80 °C temperature range are less studied for supercapacitor [38]. While a few have reported on the symmetrical supercapacitor employing ionic liquid gels electrolytes and evaluation of their electrochemical performance [39–42], similar studies on the hybrid supercapacitors with asymmetric electrodes using the ionic liquid gel electrolytes are scarce.

In this work, we have investigated supercapacitor by combining the three significant attributes, micro-porosity of the PEDOT conducting polymer electrode, a hybrid configuration using large surface area graphene asymmetric electrode, and the ionic liquid polymeric gel as high conductivity high-voltage stable electrolyte. The choice of PEDOT is made due to its high p-conductivity and wide potential window besides its chemical and structural stability relative to other conducting polymers [43]. By creating the PEDOT film in highly microporous form with pervasive access to electrolyte ions within deep interiors using

the pulsed current electropolymerization, it was possible to achieve higher areal capacitance even with a thin layer of low specific mass [44] and excellent cyclic performance when used with ionic liquid electrolytes [42, 45]. Graphene as negative electrode has the advantage of large surface area which is highly accessible to ions and is reported to show excellent energy storage performance in supercapacitor devices. In this work, the hybrid supercapacitors using the electropolymerized PEDOT and graphene electrodes were assembled with 1-butyl-3-methylimidazolium tetrafluoroborate ([BMIM][BF<sub>4</sub>]) ionic liquid gel. In the hybrid design, the energy storage is accomplished by storage of charges as the EDL capacitance at the graphene electrode and through the reversible faradic redox (doping and de-doping) process at the microporous PEDOT electrode while the increased operational potential of 2.7 V provided a boost to the energy density. Areal capacitance density > 102 mF cm<sup>-2</sup> is realized which is an improvement over the 10–20 mF cm<sup>-2</sup> reported earlier for symmetrical PEDOT supercapacitors based on ionic liquid electrolytes [45]. Further, we realized the energy density of 14.9 Wh kg<sup>-1</sup> at specific power rating of 9.8 kW kg<sup>-1</sup> which appears promising for energy storage applications in most portable electronics. Finally, the autonomous power storage application of such hybrid supercapacitors was demonstrated in an energy-harvesting circuit comprising silicon solar cell under ambient outdoor light. The storage of harvested solar electricity is realized by rapid < 100 s charging of hybrid solid-state supercapacitor and it was shown that about 50% stored energy can be retained for over 1200 s. The lightweight thin and easy fabrication of hybrid supercapacitor under ambient conditions with high energy density in conjunction with solar cells can find uses in powering portable low-power and flexible electronics [46]. This paper reports on the detailed results and discussion of these investigations.

## 2 Experimental

### 2.1 Electrode preparation

The PEDOT electrode was deposited over flexible graphite sheet by pulsed current electropolymerization of the 3, 4-ethylenedioxythiophene (EDOT, 97% Sigma Aldrich) monomer in acetonitrile medium containing 0.1 M LiClO<sub>4</sub> electrolyte and using the Pt foil as a counter electrode. The electropolymerization was carried out by applying sequential unipolar anodic current pulses of 4 mA cm<sup>-2</sup> amplitude each shaped for ultra-short ON period of 10 ms followed by the pulse OFF time of 100 ms [44, 47]. The cumulative number of current pulse cycles ranged from 10–20 k cycles which essentially determines the thickness of PEDOT film coated over graphite sheet. The uniqueness of process of PEDOT deposition lies

in the fact that monomer electropolymerization is basically carried out during the ultra-short 10 ms pulsed current ON period while the long 100 ms pulsed current OFF period is exploited in homogenization of the monomer in the vicinity of the electrode–electrolyte interface as well as to exclude any unsustainable adsorbents over the substrate surface which revert back into the medium. This way, the pulsed electropolymerization process exerts an effective control over the polymerization kinetics and hence able to produce the PEDOT film with a highly porous morphology through the control of the amplitude and on–off times of the current pulses. Following synthesis, the PEDOT film/graphite electrode was vacuum-dried overnight to ensure the complete removal of solvent. Graphene powder of < 2 μm average particle size basically comprising 4–5 layers with an average thickness of 8 nm was used for preparation of graphene electrode. The BET specific surface area and porosity parameters of the graphene powder were ~600 m<sup>2</sup> g<sup>-1</sup> and total pore volume of ~0.978 cm<sup>3</sup> g<sup>-1</sup> containing large proportion of mesoporosity with the average pore size of ~6.5 nm. The graphene electrode was coated using doctor's blade method from a slurry of graphene mixed with poly(vinylidene fluoride-hexafluoropropylene) (PVdF-HFP) binder in 9:1 (w/w) ratio in *n*-methyl-2-pyrrolidone (NMP). The coated electrodes were vacuum-dried overnight at ~100 °C before use in the fabrication of the supercapacitor cells.

### 2.2 Supercapacitor cell fabrication

The electrolyte used for supercapacitor cell fabrication was based on ([BMIM][BF<sub>4</sub>]), (> 97.0%) ionic liquid. The ionic liquid gel polymer electrolyte was formed with host polymer (PVdF-HFP, Mw 400,000) with ([BMIM][BF<sub>4</sub>]) in 20:80 weight ratio and 0.1 M LiClO<sub>4</sub> dopant in acetone. All solid-state supercapacitor cells were fabricated by casting the highly viscous ionic liquid gel (ILG) electrolyte over the PEDOT and graphene electrodes and the acetone was allowed to evaporate in dry air. The two electrodes were placed over each other and pressed slightly to form the complete capacitor cell which is stored in N<sub>2</sub>-filled glove box for ~2 h to ensure the complete evaporation of organic solvent before characterization. With the ionic liquid gel electrolyte also serving as a separator, such solid-state supercapacitor cells are compact, reliable, and free from leakage of the liquid component.

### 2.3 Characterizations

Electrochemical properties of the supercapacitor cells were analyzed by the cyclic voltammetry (CV), galvanostatic charge–discharge (CD), and ac impedance spectroscopy (EIS) techniques. The CV measurements were performed using the Solartron electrochemical interface (Model 1287) by recording the flow of electric current. The voltage was scanned from the

anodic to cathode voltage direction at different rates between 5 and 100 mV s<sup>-1</sup>. The specific capacitance,  $C_{SV}$ , of the electrodes from the CV data was determined by the relation [11, 13],

$$C_{SV} = \frac{1}{v_s m_{ac} (V_a - V_c)} \int_{V_c}^{V_a} I dV, \quad (1)$$

where  $(V_a - V_c)$  represents the anodic to cathodic potential range,  $v_s$  the voltage scan rate, and  $I$  the current response. The electrochemically active mass of the electrode  $m_{ac}$  is used in determining the specific capacitance. The CD characteristics were measured in the same cell at constant current densities between 0.25 and 2.0 mA cm<sup>-2</sup> in potential range, from 0.05 to 1.0 V. The specific discharge capacitance from the CD data,  $C_{sd}$  is determined by the relation,

$$C_{sd} = \frac{I_d \cdot \Delta t_d}{m_{ac} \cdot \Delta V_d}, \quad (2)$$

where  $I_d$  is the constant discharge current density,  $\Delta t_d$  is the discharge time, and  $\Delta V_d$  is the voltage change on discharge measured after excluding the IR voltage drop. The ac impedance spectra were recorded in a two-electrode cell configuration in the frequency range 0.01 Hz–100 kHz with ac signal amplitude of 10 mV using the Solartron gain-phase impedance analyzer (Model: 1260). The impedance data provide frequency dependence of the real  $Z_{Re}$  and imaginary  $Z_{Im}$  impedances. The Nyquist plots between  $Z_{Re}$  and  $Z_{Im}$  based on the impedance data were simulated using the electrical equivalent circuit model representing the electrochemical and electrophysical properties of the EDL graphene and Faradaic PEDOT electrodes using the Z-plot software (Scribner Associate) which provided the characteristic resistances and various contributing factors to the capacitance. The overall supercapacitor cell capacitance from the impedance study,  $C_i$  is obtained by the relation,  $C_i = (2\pi f Z_{Im})^{-1}$ , where  $f$  is the signal frequency. The energy density,  $E_D$  and power density  $P_D$  of the supercapacitor cell were calculated from the CD data using the relations [11, 13],

$$E_D = \frac{1}{2} \cdot C_{sd} (V_d)^2 \quad (3)$$

$$P_D = \frac{(V_d)^2}{4m_{ac} \cdot ESR}. \quad (4)$$

Here, ESR refers to the equivalent series resistance of the supercapacitor cell given as,

$$ESR = \frac{V_{drop}}{2 \cdot I_d}, \quad (5)$$

where  $V_{drop}$  is sudden voltage drop at the start of the discharge curve due to internal resistance and the other terms  $V_d$ ,  $I_d$ ,  $C_{sd}$ , and  $m_{ac}$  are defined earlier as the supercapacitor cell voltage, discharge current density, specific discharge capacitance of supercapacitor cell given by Eq. (2), and electroactive electrode mass, respectively.

## 3 Results and discussions

### 3.1 Bonding structure of electrodes using Raman spectroscopy

The synthesis of PEDOT electrode by the electropolymerization process was confirmed by probing the bonding structure of the PEDOT electrode using the Raman scattering spectra. The Raman spectra shown in Fig. 1a show a consistent match of all peaks with corresponding Raman spectrum of the chemically synthesized PEDOT [48]. The most intense peak at 1436 cm<sup>-1</sup> is attributed to the  $C_\alpha=C_\beta(-O)$  symmetric stretching vibrational modes and the asymmetric  $C_\alpha=C_\beta$  stretching modes are identified by peaks at 1498 and 1559 cm<sup>-1</sup>. This shows that in the electropolymerization process, the PEDOT film formation involves long-chain linkage by  $\alpha$ - $\beta$  couplings. In this case, the linkages at the  $\beta$ -position become feasible via progressive delocalization of the unpaired electrons [49]. Raman peaks at 1365 and 1261 cm<sup>-1</sup> correspond to the  $C_\beta-C_\beta$  and  $C_\alpha-C_\alpha'$  inter-ring stretching modes, respectively. This suggests that the cation radical association is also by the linkage at  $\alpha$ - $\alpha'$  (5, 5') position which indicates short-chain PEDOT oligomers wherein the molecular structure is dominantly in the transconfiguration with highly regiochemical order [50]. By analogy, the PEDOT films formed by current pulses polymerize into a mixture of low molecular weight oligomers along with longer-chain polymer units and together these are responsible for its microporous microstructure as shown later in Fig. 1c. Additional peaks at 1120 and 700 cm<sup>-1</sup> are assigned to the C-O-C and C-S-C deformations, respectively. The inset shows peak at 987 cm<sup>-1</sup> which originate from oxyethylene ring deformation. The  $ClO_4^-$  ion conjugation during the PEDOT growth is revealed by broad peak at  $939 \pm 6$  cm<sup>-1</sup> based on the Raman peaks of free  $ClO_4^-$  at 934 cm<sup>-1</sup>, and ion pairs,  $[Li^+ClO_4^-]$  at 948 cm<sup>-1</sup> [51]. The anion ( $ClO_4^-$ ) association within the growing chain network is due to the positive charge in molecular subunits of the chain thereby creating doped state of PEDOT. The long (100 ms) pulse off period used in the electropolymerization therefore enables a higher degree of dopant conjugation by  $ClO_4^-$  diffusion from the solution phase since during this period no further growth of PEDOT molecular units takes place.

Raman spectrum of graphene electrode shown in Fig. 1b shows two main peaks at 1562 and 2684  $\text{cm}^{-1}$ . These peaks are, respectively, identified as the G band due to the in-plane vibrational modes and the G' (2D) band attributed to a second-order overtone of a different in-plane vibration of the  $sp^2$  carbon-carbon bonds arranged in the hexagonal network. In the standard Raman spectra of the monolayer graphene, the G band appears at 1582  $\text{cm}^{-1}$ . The observed red-shift here in G band is due to the multilayer graphene stacking [52]. The G' (2D) band is known to show broadening and higher wavenumber shift as the graphene layer stacking increases finally approaching the graphite-like structure. The sharp and intense G' (2D) band observed for graphene electrode is consistent with its few-layer graphene structure. The third major Raman peak at 1336  $\text{cm}^{-1}$  occurring at nearly half the wavenumber position of the 2D is due to the disorder-induced D-band. The lower intensity ratio  $I_D/I_G < 1$  indicates disorder is not large [53]. It is known that with the increase in the disorder, the Raman spectrum of graphene shows two additional peaks; D' at 1620  $\text{cm}^{-1}$  and combination of D+G peak at 2940  $\text{cm}^{-1}$  [54]. In the Raman spectrum of the graphene electrode, we observed only the

low-intensity D+G band at 2910  $\text{cm}^{-1}$  due to dispersion effects of D and G' (2D) bands.

### 3.2 Microstructure

The surface morphology of the PEDOT and graphene electrodes is revealed by scanning electron micrographs (SEM) presented in Fig. 1c and d, respectively. It is apparent that the pulsed current electropolymerization results in a highly porous microstructure of the PEDOT film over flexible graphite. The SEM image in Fig. 1c depicts thin wrinkly flakes forming distributed clusters spread across the substrate surface. These clusters have ridge-like stacking of flakes which arise as the PEDOT electropolymerization process is interrupted periodically by the ON-OFF current pulsed cycles [44, 47]. Further, these flake-like clusters are conjoined by PEDOT fibers forming deep 50–70 nm size voids between these clusters which imparts a highly porous morphology to the whole PEDOT film. This is important for deep and pervasive electrolyte ion access when used with ionic liquid gel electrolyte in achieving higher specific capacitance in solid-state design of the supercapacitor. Such microstructural features are consequence of

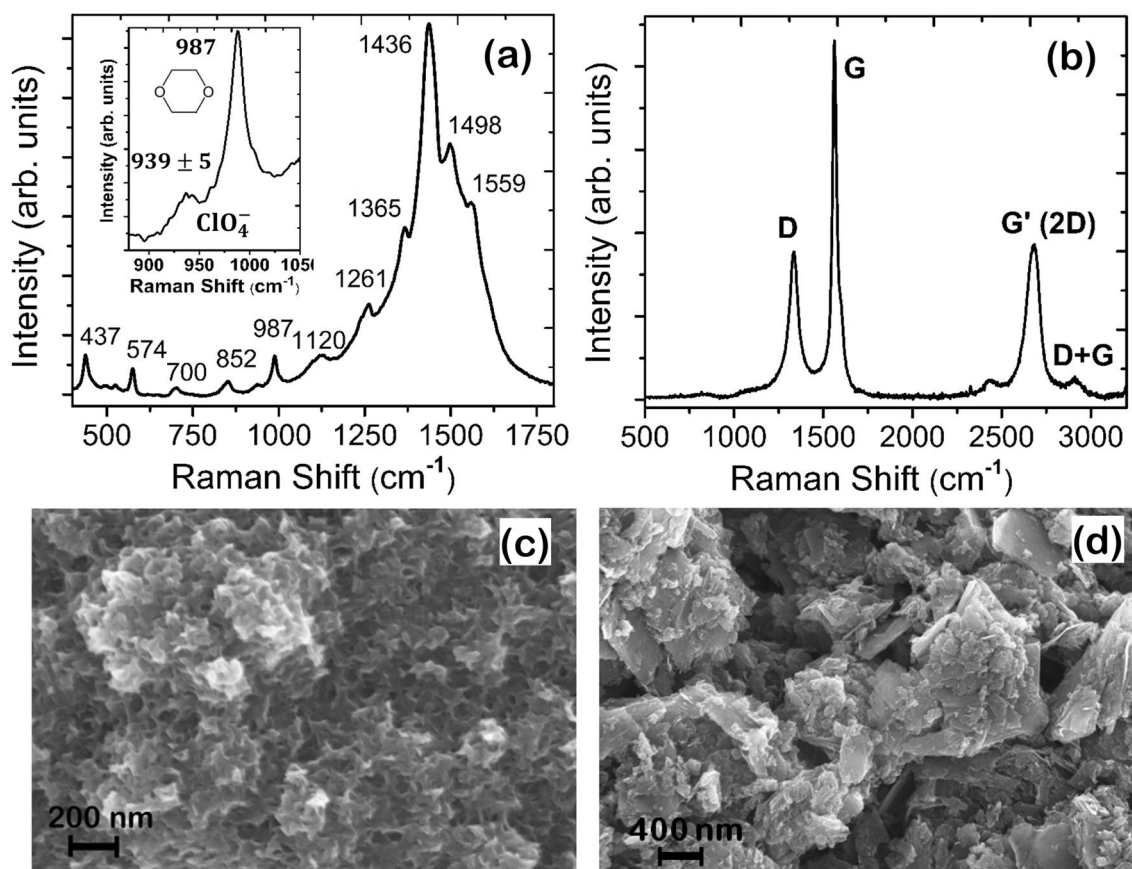


**Fig. 1** Raman spectra of **a** electropolymerized PEDOT and **b** slurry-coated graphene electrodes. Scanning electron microscopy images showing morphology of **c** electropolymerized PEDOT and **d** slurry-coated graphene electrodes

short-term pulsed polymerization in which first the EDOT monomer species rapidly oxidize forming  $[\text{EDOT}]^+$  cation radicals that instantaneously nucleate in significantly large number over substrate sites. These radical stabilize by coupling and chain linkages by deprotonation forming short-chain PEDOT molecular units confirmed by Raman analysis (Fig. 1a), and thus form fibrous bundles across the substrate surface at random sites. Their growth is limited by the number of cation radicals linked in the short 10 ms current ON period. In the next 100 ms long pulsed current OFF periods, the growth of PEDOT molecular units is terminated as no new cation radicals form but the EDOT monomer species at the substrate vicinity is replenished by diffusion in the solution. With sufficient monomer units at the substrate, a similar sequence follows in the next pulsed current ON time at fresh sites as the chain linkages in the previous current cycles are frustrated which results in the formation of new PEDOT fibrous bundles on top of each other thus creating a ridge-like morphology as shown in Fig. 1c. The graphene electrode morphology shows laminar chunks of graphene with average lateral size ranging 0.5–1.8  $\mu\text{m}$ . Their random distribution is conducive for creating interlaminar spaces which are easily accessed by ionic liquid electrolyte thereby exposing them to vast surface area. This is highly desirable for enhancing electric double-layer capacitance.

### 3.3 PEDOT and graphene symmetrical supercapacitors: electrochemical capacitance

Initially, the capacitive properties of the PEDOT and graphene electrodes were individually determined for later integration in a hybrid supercapacitor device. This was done by measuring the electrochemical properties of the PEDOT electrode in the positive and of the graphene electrode in the negative voltage range each individually configured as the symmetrical supercapacitor device with ionic liquid gel electrolyte. The high conductivity of p-doped PEDOT in the oxidized state is most useful as a positive electrode [37]. Since, PEDOT at a negative potential of  $-0.2$  V remains in the doped state, the CV plots of the PEDOT/ILG/PEDOT supercapacitor were studied in  $-0.2$ – $+1.0$  V range and the results are shown in Fig. 2a. The charge storage activity evidenced from quasi-rectangular nature of the CV plots is due to redox process representing the doping and de-doping of the  $\text{ClO}_4$  anions of ionic liquid gel electrolyte into micro-pores of PEDOT. At high scan rates  $\geq 70$   $\text{mV s}^{-1}$ , the rapid increase in current and a slight deviation from the rectangular nature of CV plots is due to diffusion limitation of the anions. The areal capacitance  $C_p$  measured from the CV curves is  $134$   $\text{mF cm}^{-2}$ . Figure 2b shows the CV plots of graphene/

ILG/graphene symmetrical supercapacitor with ionic liquid gel electrolyte measured in the negative ( $-1.0$  to  $0$  V) potential window. Herein, the typical rectangular CV plots show contribution from the electric double-layer formed at vast interface of graphene with the ionic liquid gel electrolyte. The areal capacitance  $C_G$  based on the CV plots at  $10$   $\text{mV s}^{-1}$  scan rate is  $40$   $\text{mF cm}^{-2}$ .

### 3.4 PEDOT/ILG/graphene hybrid supercapacitor with variable PEDOT thickness

Both graphene and PEDOT electrodes in the symmetrical supercapacitor structure have shown substantive electrochemical capacitive behavior in the negative and positive biased conditions, respectively, and high-charge transfer rate ability for pairing in the hybrid supercapacitor configuration. The criterion commonly used in the assembly of the hybrid supercapacitor device is to equally balance the charges stored by the individual electrode in order to achieve high specific capacitance. The charge is given by  $Q_{n,p} = m_{n,p} \cdot A_{n,p} \cdot \Delta E_{n,p} \cdot C_{n,p}$ , where the suffixes n and p denote the negative and positive bias at the active electrodes graphene and PEDOT, respectively, and  $Q$ ,  $m$ ,  $A$ ,  $C$  and  $\Delta E$  are the charge, electroactive active mass, electrode area, areal capacitance density, and the operating voltage range of the electrodes, respectively. The areal capacitance density of individual microporous PEDOT and graphene electrodes for the charge balance was estimated from the symmetrical supercapacitor areal capacitance as  $2C_p$  and  $2C_G$ , respectively, based on the CV data shown in Fig. 2. Since the symmetrical supercapacitor data were obtained using the ionic liquid gel electrolyte, this provided more realistic areal capacitance values for both PEDOT and graphene electrodes in order to achieve the charge balance in the hybrid supercapacitor cells. The hybrid solid-state supercapacitor is designed with physically overlapping PEDOT and graphene electrodes of same area. With pseudo-capacitive PEDOT electrode showing higher areal charge density compared to EDLC graphene electrode, the conventional past approach of increasing the EDLC electrode mass in order to compensate for the deficiency in its specific capacity may not work well in the solid-state cell configuration. The EDLC is based on the interfacial storage mechanism and just the increase in the areal mass may not ensure a proportionate increase in the electroactive surface area in contact with the gel electrolyte which is essential to increase the charge storage on the electrode. An overriding factor not considered in the past is the vastly different charge transfer kinetics of both electrodes rooted in faradic and double-layer mechanisms as it affects the charge–discharge function of the hybrid supercapacitor. In PEDOT electrode, the anions locate along the backbone of the molecular chains and diffuse into and from the interiors

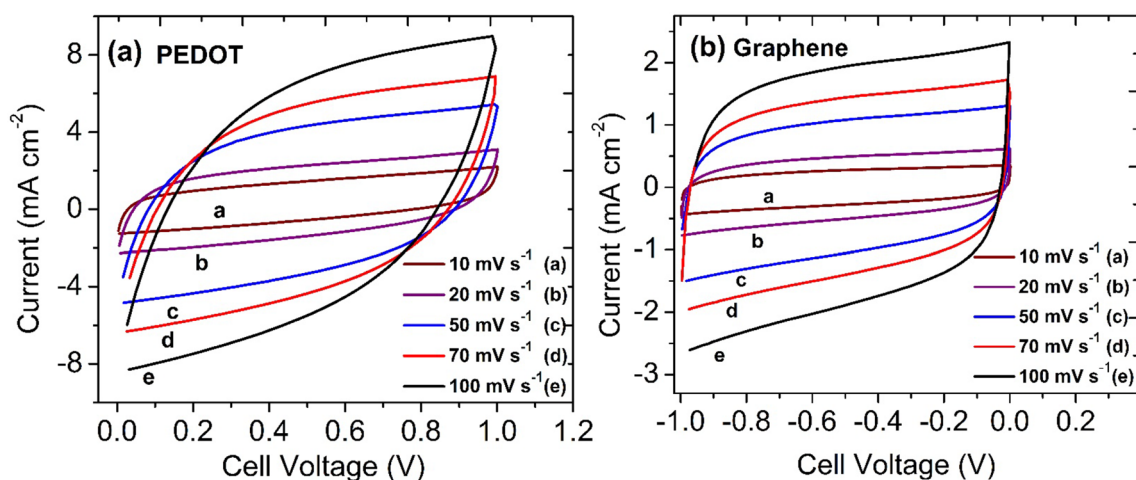


**Fig. 2** CV plots at various scan rates of **a** PEDOT and **b** graphene symmetrical solid-state supercapacitors using ionic liquid gel polymer electrolytes

of the chains network within its microporous morphology during the doping and de-doping processes, whereas in graphene, the charge transfer occurs at the graphene platelets surface in contact with the electrolyte ions. This difference could reflect on the asymmetry in the charge–discharge behavior of the hybrid supercapacitor device. In the controlled pulsed electropolymerization process for PEDOT synthesis, such as used in this work, it is possible to achieve the change in areal mass without affecting the PEDOT electrode morphology and hence maintain the same pervasive access to electrolyte ions and ion kinetics [44]. We have therefore fabricated three test structures of the hybrid supercapacitor devices using the graphene electrode of constant mass and instead employed the PEDOT electrode of different thicknesses obtained by changing the number of pulsed current cycles used in the electropolymerization deposition which resulted in different mass loading of the PEDOT electrode. Figure 3a–d shows the CV plots, specific capacitance, impedance spectra, and the charge–discharge curves of the hybrid supercapacitor devices having the PEDOT to graphene electrode mass ratio 0.35, 0.46, and 0.78 denoted as the hybrid supercapacitor (HSC) devices HSC-A, -B, and -C, respectively. The CV plots shown in Fig. 3a recorded at  $70 \text{ mV s}^{-1}$  in the potential range  $-0.2 \rightarrow +1.5 \text{ V}$  have quasi-rectangular shape characterizing its charge storage properties. Figure 3b shows the voltage scan rate dependence of the areal capacitance density evaluated from CV plots using Eq. (1). The hybrid supercapacitor HSC-B with PEDOT/graphene mass ratio of 0.46 yields highest specific capacitance of  $77.8 \text{ mF cm}^{-2}$  compared to  $53.8$  and  $50.1 \text{ mF cm}^{-2}$  for HSC-A and -C, respectively, measured at  $10 \text{ mV s}^{-1}$ . The hybrid supercapacitors HSC-A and -B show a steep reduction in areal capacitance responding to an early increase in

the scan rate compared to the HSC-C device with PEDOT/graphene mass loading of 0.78 which shows intermediate specific capacitance but a much steadier change with the voltage scan rate. It is apparent that HSC-A and -B supercapacitor devices show diffusion limitation due to asynchronous charge transfer relative to the electronic response, whereas the diffusion limitation is not as acute for HSC-C device even though it has a relatively thicker PEDOT film. This is attributed to the increase in the conductivity of the PEDOT electrode in HSC-C as evidenced from the impedance data shown as Nyquist plots in Fig. 3c. Steep rise of the imaginary impedance at lower frequency shows capacitive behavior for each of the hybrid supercapacitor devices. The high-frequency response in the inset of Fig. 3c shows real-axis intercept which represents the overall decrease at  $67$ ,  $35$ , and  $18 \Omega \text{ cm}^2$  in the electrical resistance of the electrode–electrolyte system with increasing mass loading of the PEDOT electrode as in HSC-A, -B, and -C, respectively. The high-frequency Nyquist plot of HSC-B device shows a semicircle response which is due to the charge transfer resistance arising from the limitation of diffusion of anions across the PEDOT-ionic liquid gel electrolyte. This is consistent with the inference from the CV plots and the scan rate dependence of specific capacitance shown in Fig. 3a and b, respectively. The HSC-C device with PEDOT/graphene ratio of 0.78 showed lowest electrode–electrolyte resistance and as the high-frequency arc-like features are hardly observed, apparently it has no significant charge transfer resistance limitation. The charge–discharge ability of the three devices was evaluated over  $0.05\text{--}1.0 \text{ V}$  window at  $0.5 \text{ mA cm}^{-2}$  current density. The most prominent effect is seen in the Coulomb efficiency. The HSC-A device shows sluggish charging due to ion diffusion limitation owing to high resistance and

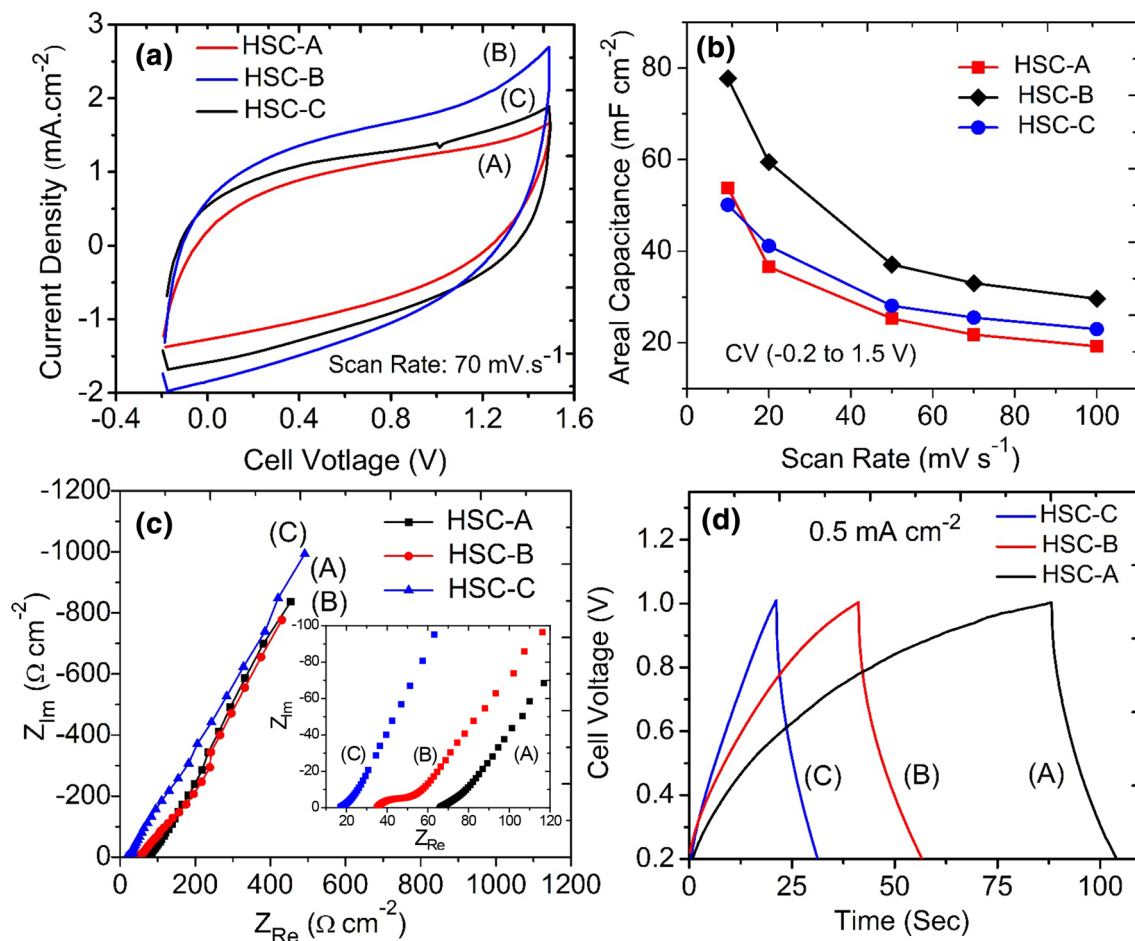


**Fig. 3** Electrochemical properties of hybrid PEDOT/ILG/graphene supercapacitors of different electrode mass ratios **a** CV plots **b** areal capacitance versus scan rate **c** Nyquist plots with inset showing expanded high-frequency region and **d** CD plots at current density of  $0.5 \text{ mA cm}^{-2}$

fast discharge attributed to large equivalent series resistance (ESR) causing poor Coulomb efficiency of 30%. For the HSC-B device, the Coulomb efficiency improves to 73.8%. The CD curves for HSC-C device are linear during charge–discharge cycles and shaped as isosceles triangle which is reflective of the capacitive property with least diffusion limitation and high Coulombs efficiency of 87%. This study showed that the overall functional performance of the hybrid supercapacitor is best evaluated from balancing of the charge on both electrodes as well as in the matching of the ion transfer kinetics as evidenced by the charge and discharge processes of both electrodes. The former is important to boost the energy density via increase in specific capacitance and the later in the power density of the hybrid supercapacitor devices.

### 3.5 Electrochemical properties of charge-balanced PEDOT–graphene hybrid supercapacitor

Figure 4a shows the representative CV plots at  $10 \text{ mV s}^{-1}$  scan rate of the PEDOT and graphene symmetrical ionic liquid gel electrolyte-based solid-state supercapacitors in the positive and negative voltage ranges, respectively, configured on the basis of mass ratio parameter evaluated through HSC-C device as discussed earlier. The CV plots testify that both electrodes are closely though not perfectly charge-balanced but more importantly are matched in charge transfer kinetics and therefore ideally disposed for pairing in the hybrid supercapacitor design. An optimally performing hybrid supercapacitor device HSC-O was fabricated based on the parameters of HSC-C device using the ionic liquid gel electrolyte of controlled thickness of  $\sim 54\text{--}60 \mu\text{m}$  with  $0.2\text{M LiClO}_4$  doping. In fabricating the supercapacitor device the asymmetrical PEDOT and graphene electrodes were wetted by  $([\text{BMIM}][\text{BF}_4]) + \text{PVDF}$  gel electrolyte and glued together by light pressing. The electrochemical energy



storage functionality of the HSC-O device was investigated by measuring the CV properties at different cell voltages, CD curves at different current densities, and electrochemical impedance spectra and the data were analyzed to obtain specific capacitance and energy–power density parameters. Figure 4b, c shows typical CV plots recorded over wide potential range from  $-0.2$  to positive  $1.5$ ,  $2.0$  and  $2.5$  V and from  $-1$  to  $+1$  V at scan rates  $20$  and  $50$   $\text{mV s}^{-1}$ , respectively. The CV plots have quasi-rectangular shape over wide potential window and are highly symmetrical about the zero voltage axis. This shows that the hybrid PEDOT/ILG/graphene supercapacitor in the solid-state structure has capacitive property and operative voltage range of  $2.7$  V. Figure 4d shows that the specific capacitance calculated from the CV plots at  $20$  and  $50$   $\text{mV s}^{-1}$  scan rates scales up with the operating potential following the empirical relation,  $C \propto V^{1.45}$  and  $C \propto V^{1.05}$ , respectively. Typically, for a potential window of  $1.7$  V, specific capacitance of  $60$   $\text{mF cm}^{-2}$  is obtained which increases to  $102$   $\text{mF cm}^{-2}$  at  $2.7$  V measured at  $20$   $\text{mV s}^{-1}$  scan rate. Notably, the CV plots show a sharp

and near vertical transition of current at a rapid rate on voltage reversal at the end of the anode cycle which indicates rapid charge transfer kinetics. This is attributed to the combination of fast ion transfer at the electrified double-layer interface with the large surface area graphene and ion diffusion across the micro-pores in the PEDOT electrode during the de-doping process.

The charge transfer kinetics aspect is further elucidated by the CV plots in the voltage range  $-1$  to  $+1$  V,  $-0.2$ – $5$  V,  $-0.2$ – $2.0$  V, and  $-0.2$ – $2.5$  V recorded at increasing  $10$ – $100$   $\text{mV s}^{-1}$  voltage scan rates shown in Fig. 5a–d, respectively. The quasi-rectangular features of the CV curves in the anodic and cathodic voltage scans are retained even at higher scan rates without any noticeable distortion which affirms to a high degree of reversibility of the stored charge in the hybrid supercapacitor. As evidenced in most supercapacitor devices, the CV plots with the increase in the scan rates show an increase in the current, which is attributed to the diffusion limitation of ions not synchronous with the much faster electronic processes. As a result, the apparent

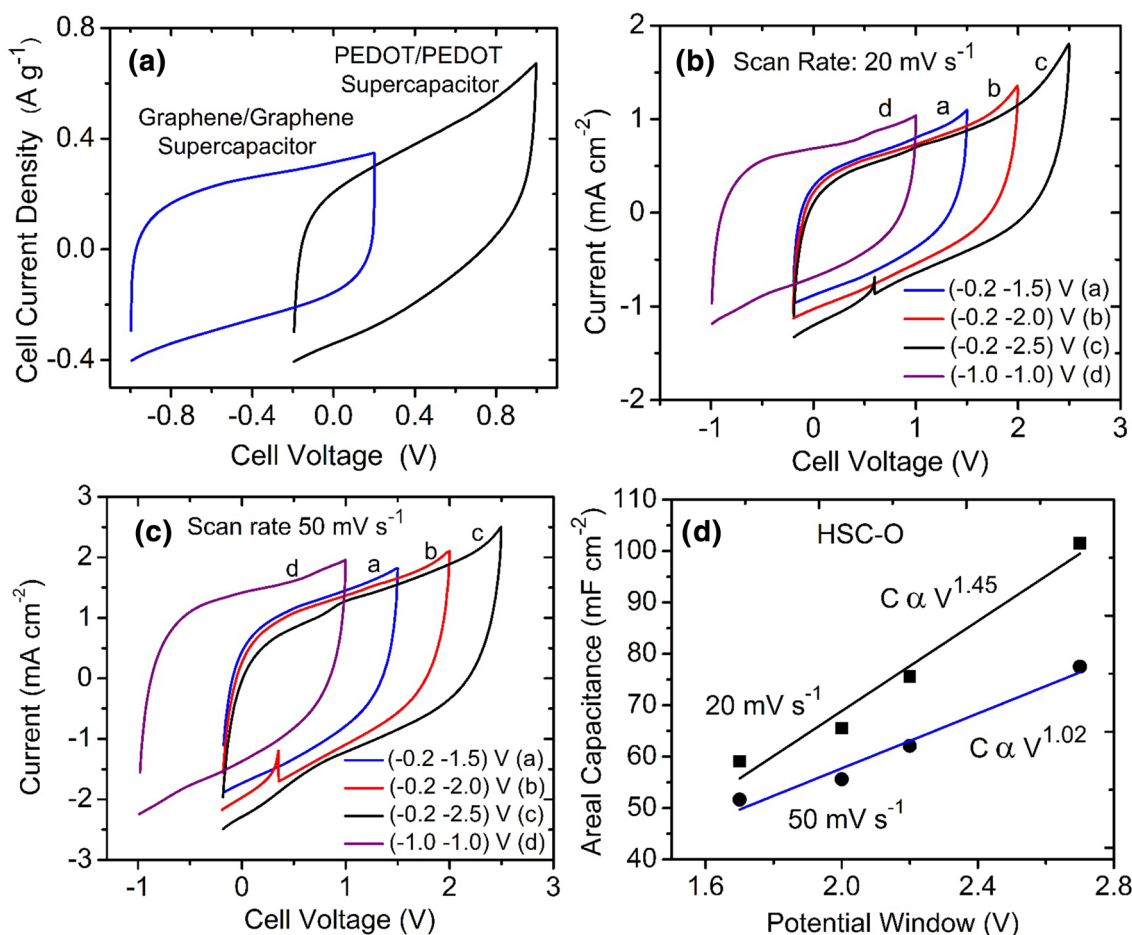


**Fig. 4** a CV plots of symmetrical graphene/ILG/graphene and PEDOT/ILG/PEDOT supercapacitors with balanced electrode charge. CV plots of hybrid PEDOT/ILG/graphene supercapacitor device

HSC-O in different voltage ranges at scan rates; **b**  $20$  and **c**  $50$   $\text{mV s}^{-1}$  and **d** linear scaling of areal capacitance with voltage for  $20$  and  $50$   $\text{mV s}^{-1}$  scan rates

specific capacitance shows a downward trend with increasing scan rate as shown in Fig. 6a. For the PEDOT electrode, such diffusion limitation could arise as the anions infiltration through the micro-pores tend to somewhat lag behind in response to the extraction of electron at a faster rate. The observation of a faster reduction in specific capacitance for supercapacitor operating at higher supercapacitor voltages (Fig. 6a) supports this conclusion as a deeper ingress of anions at higher voltages will encounter a slower diffusive path in the de-doping process step. In the case of graphene electrode, the reduced access of ions to the vastly expanded interface with electrolyte ions appears to be the reason. The curves shown in Fig. 6a are reflective of the combined effect of the two electrodes on the capacitive property of the supercapacitor device. The specific capacitance at the lowest scan rate provides the intrinsic energy storage capacity of  $71.4 \text{ F g}^{-1}$  at 2.7 V which is significantly high for the supercapacitors in the solid-state configuration.

Evidently, the diffusivity of ions is critical for realizing high specific capacitance especially for charge storage in

supercapacitors on solid-state platform. Randles–Sevcik analysis was performed on the HSC-O asymmetric supercapacitor with ionic liquid gel electrolyte in order to establish a correlation between the ion diffusivity and the electron mobility. The scan rate dependence of the peak anodic and cathodic currents  $I_{PA}$  related to the parameter  $D$  representing apparent charge transfer diffusion coefficient or diffusivity is given by the Randles–Sevcik equation,

$$I_{PA} = 0.6104 \cdot n^{1.5} \cdot F \cdot c \cdot A \cdot \sqrt{FD/RT} \cdot \sqrt{\nu} \quad (6)$$

where  $c$  denotes the active ionic specie concentration in electrolyte;  $n$  the number of electrons involved in the reduction process;  $F$  is the Faraday number;  $R$  the ideal gas constant;  $\nu$  the scan rate in  $\text{V s}^{-1}$ ;  $A$  the electrode area; and  $T$  the temperature in K. Figure 6b shows the linear dependence of the peak anodic current  $I_{PA}$  versus  $\sqrt{\nu}$  for all supercapacitor cell voltage ranges consistent with the Randles–Sevcik Eq. (6) and provides the diffusivity  $D$  as  $6.6 \times 10^{-9} \text{ cm}^2 \text{ s}^{-1}$  at a potential 2.7 V attributed to  $\text{ClO}_4^-$  anions. The diffusivity values

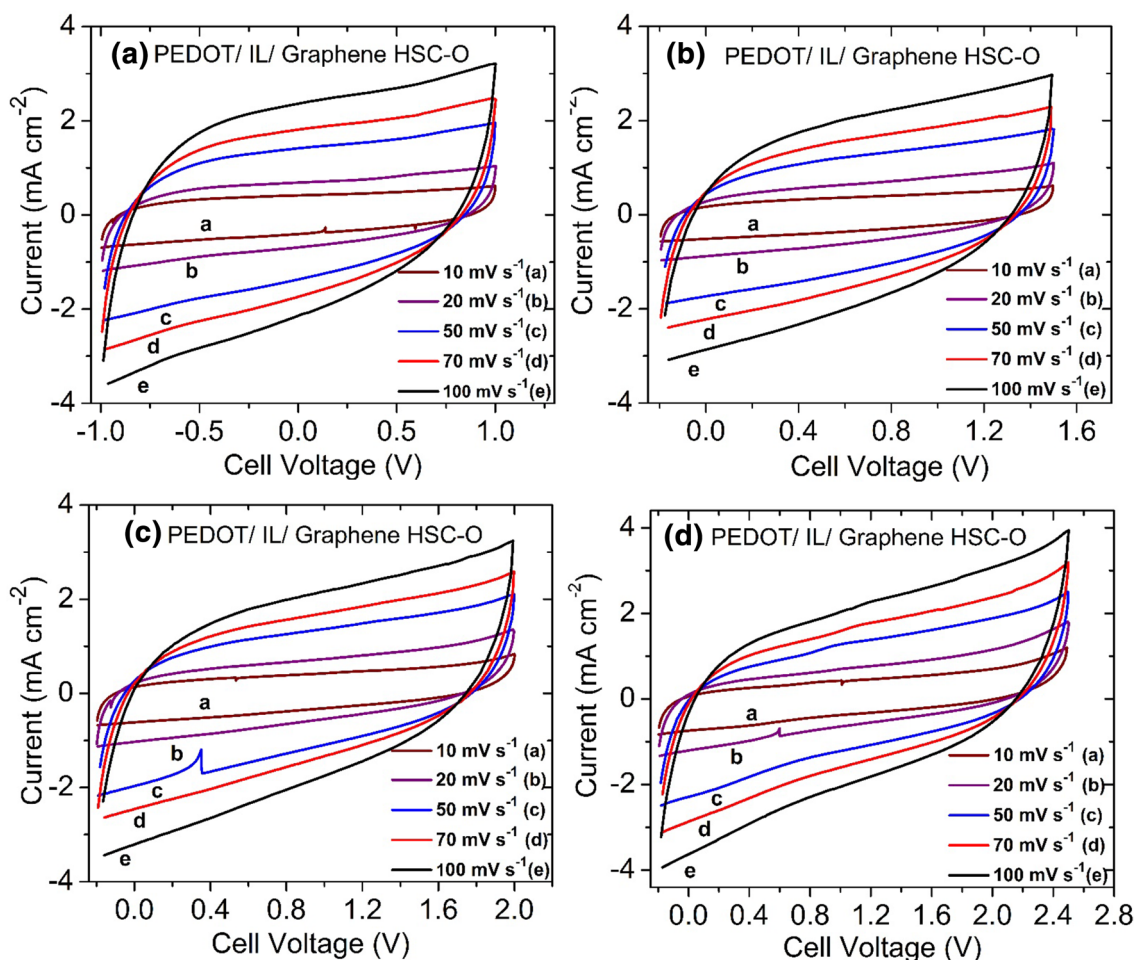


**Fig. 5** Scan rate dependence of CV plots of PEDOT/ILG/graphene hybrid supercapacitor device HSC-O in different voltage ranges **a** –1 to +1 V, **b** –0.2 to +1.5 V **c** –0.2 to +2.0 V, and **d** –0.2 to +2.5 V

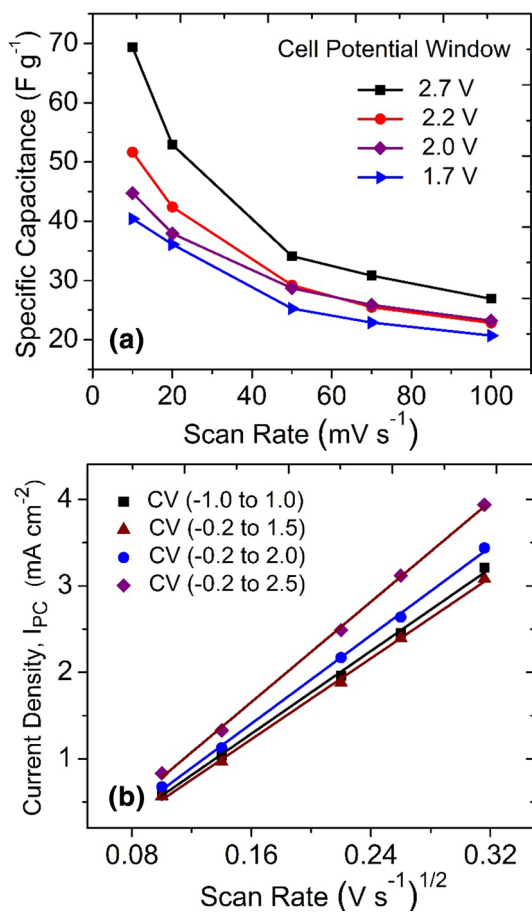


**Fig. 6** For PEDOT/ILG/graphene hybrid supercapacitor device HSC-O, **a** variation of areal capacitance density of with scan rates in different voltage ranges **b** Randels–Sevcik plot showing linear variation of peak cathode current with square root of scan rates

are comparable with those in liquid electrolytes and show a decrease with the cell potential as  $5.0 \times 10^{-9}$ ,  $4.3 \times 10^{-9}$ , and  $4.0 \times 10^{-9}$  cm<sup>2</sup> s<sup>-1</sup> at cell voltages 2.2, 2.0, and 1.7 V, respectively, which mainly relates to the anodic process of in-diffusion of ions within the microporous PEDOT. Figure 7a, b shows the charge–discharge (CD) characteristics of the charge-balanced hybrid supercapacitor device (HSC-O) measured at current densities 0.5–2.0 mA cm<sup>-2</sup> ramping up the cell potential to 1.0 V. The CD curves at all current densities are near linear, and triangular in shape which show high capacitive charge storage attributes of the hybrid supercapacitor cell. The device functional aspects of the hybrid supercapacitor cell are better described by the energy density  $E_D$  and power density  $P_D$  parameters which were calculated from the CD data using the Eqs. (3–5). The Ragone plot shown in Fig. 7c of energy–power density dependence of the PEDOT/ILG/graphene hybrid supercapacitor device HSC-O shows the maximum energy density of 14.9 Wh kg<sup>-1</sup> at power density 9.8 kW kg<sup>-1</sup>. The widely varying energy

density in the range 14.9–5.8 Wh kg<sup>-1</sup>, with corresponding nominal change in the power density in the range from 9.8 to 10.8 kW kg<sup>-1</sup>, implies that the maximum power delivery from the solid-state supercapacitor device is restricted on the average to  $\sim 10.3$  kW kg<sup>-1</sup>. This is attributed to high and near invariant ESR value on the discharging rate. Even though a higher energy density is attained by slow charging rate, on discharge at the same or higher discharge rates, the ESR limits the power between 9.8 and 10.8 kW kg<sup>-1</sup> that can be delivered to the load. In the PEDOT/graphene hybrid supercapacitor device HSC-O, the main contribution to the ESR values originates from the intrinsic resistance of the electrode and contacts. However, the internal resistance encountered by ions in diffusion through ionic gel electrolyte could also be a factor which is due to non-optimized LiClO<sub>4</sub> electrolyte dopant incorporation.

The energy–power density values realized here for the PEDOT/ILG/graphene hybrid supercapacitor in the solid-state form using the ionic liquid gel electrolyte are quite encouraging when compared with the aqueous electrolyte hybrid supercapacitors based on the asymmetric conducting polymer paired with metal oxide or carbon electrodes. The energy density values of 13.5, 7.4, and 14.9 Wh kg<sup>-1</sup> have been reported for MnO<sub>2</sub> paired with PEDOT [17], polypyrrole [17], and graphene [55] asymmetric supercapacitors, respectively. Similarly, the aqueous hybrid supercapacitors with PEDOT using carbon maxsorb [17] and carbon nanofoam [26] as second asymmetric electrode showed energy density of 3.82 and 13.6 Wh kg<sup>-1</sup>, respectively, and somewhat higher energy density of 20 Wh kg<sup>-1</sup> using composite electrodes of graphene-carbon nanotubes with conducting polymers [56]. The fewer studies reported on hybrid supercapacitors in the solid-state design using metal oxides or composites with the other asymmetric graphene or conducting polymer electrode are all based on polymeric gel electrolytes [57]. The energy and power density values reported for MnO<sub>2</sub>@ PEDOT/LiClO<sub>4</sub>-PMMA gel /PEDOT supercapacitors [58] as 9.8 and 0.85 kW kg<sup>-1</sup> and CNTs-MnO<sub>2</sub>/Na<sub>2</sub>SO<sub>4</sub>-PVP gel/CNTs/PANI [59] as 24.8 and 0.12 kW kg<sup>-1</sup>, respectively, are much smaller compared to the PEDOT/ILG/graphene hybrid supercapacitor HSC-O device. Using the complex graphene (IL-CMG)/H<sub>2</sub>SO<sub>4</sub>-PVA gel/RuO<sub>2</sub>-IL-CMG asymmetric electrodes, the energy and power densities of 19.7 and 6.8 Wh kg<sup>-1</sup>, respectively, have been reported [60], which is comparable to our results on HSC-O supercapacitor device. The improved energy density in PEDOT/ILG/graphene hybrid supercapacitor HSC-O device is ascribed to optimum access to the electrolyte ions within microporous PEDOT with open voids and graphene which presents a much larger interface for ions. The limitation of power is essentially due to intrinsic cell resistance and least impact from ionic diffusion resistances as evident

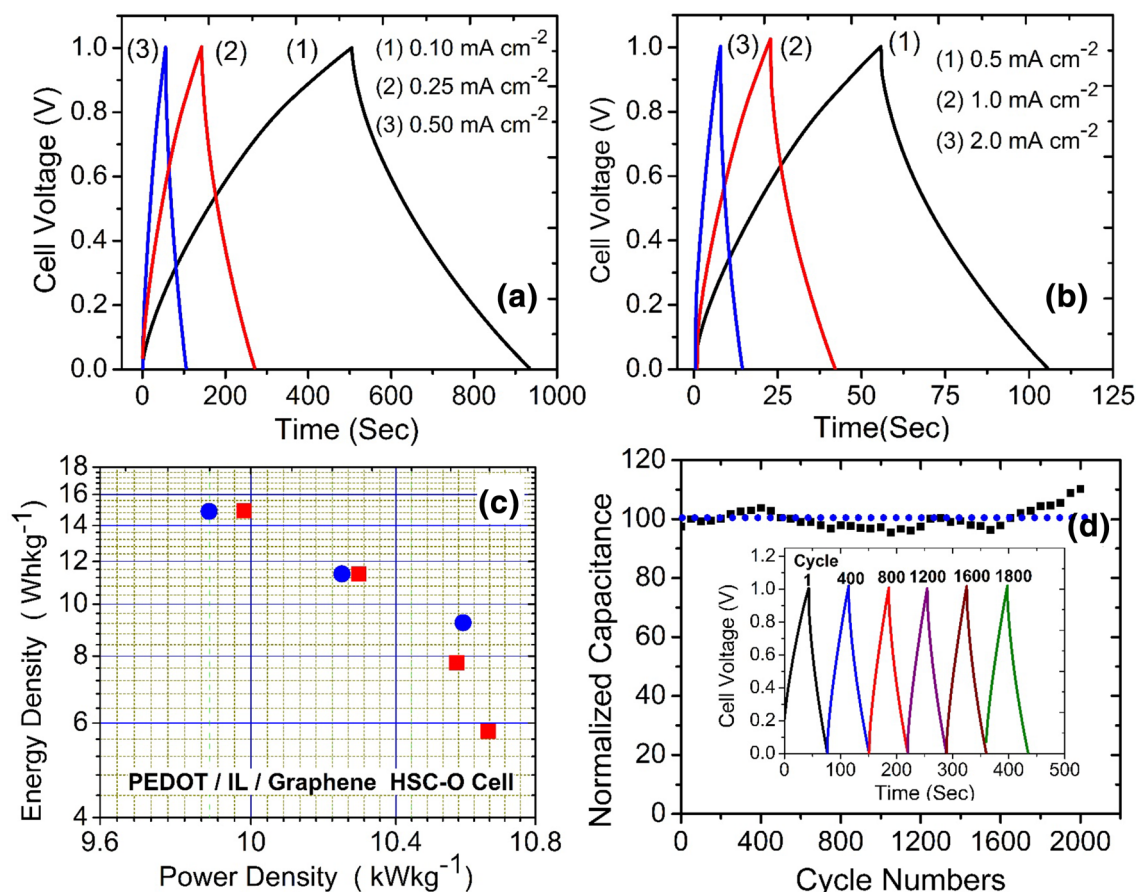


**Fig. 7** For PEDOT/IL/graphene hybrid supercapacitor device HSC-O, **a** CD plots at current density 0.1, 0.25, and 0.5 mA cm<sup>-2</sup> **b** 0.5, 1.0, and 2.0 mA cm<sup>-2</sup> **c** energy versus power density plot **d** cycling performance with CD plots after certain number of cycles in inset

from impedance and Bode plot analysis of the hybrid supercapacitor described later in the following sections.

Cyclic stability of the hybrid supercapacitor cell HSC-O cell was tested by applying 2000 continuous charge–discharge cycles at constant current density of 0.5 mA cm<sup>-2</sup>. Figure 7d shows the variation of the discharge areal capacitance as a function of the cycle number normalized to the initial value. The areal capacitance values represent an almost stable trend varying randomly within  $\pm 5\%$  of the starting value that confirms the stability of PEDOT/IL/graphene hybrid supercapacitor. After testing continuously for 1600 CD cycles, the supercapacitor testing was recommenced for additional 400 CD cycles. It is interesting to note that the areal capacitance density gradually increases up to 2000 test cycle. This is attributed to relaxation and homogenization of the dopant ions within the electrode matrix. Inset shows the CD plots after each 400 test cycles. These show Coulombic efficiency of the charge–discharge is almost stable over continuous 2000 charge–discharge cycles.

### 3.6 AC impedance spectra of PEDOT/IL/graphene hybrid supercapacitor

Electrical attributes of the electrode/electrolyte interface and the nature of the diffusive ion transport at the interface in the PEDOT/IL/graphene hybrid supercapacitor device HSC-O were determined using the electrochemical impedance spectroscopy (EIS). The impedance spectrum was recorded using a sinusoidal ac signal of 10 mV amplitude in the frequency range 100 kHz–0.01 Hz with the hybrid supercapacitor separately charged to 0.5 and 1.0 V by applying mean dc bias as well as when not charged (0 V dc bias). The impedance data were analyzed as Nyquist plots between the real  $Z_{Re}$  and imaginary  $Z_{Im}$  impedances measured at these frequencies, and the results are shown in Fig. 8a. The electrical equivalent circuit representing the hybrid supercapacitor system is shown in the inset of 8a. The series resistive circuit component  $R_B$  represents the bulk resistance due to electrolyte, electrode, and contacts. The capacitive component are the double-layer capacitance,  $C_{dl}$  and pseudocapacitance,  $C_{psuedo}$  due to graphene and PEDOT electrodes in parallel with the

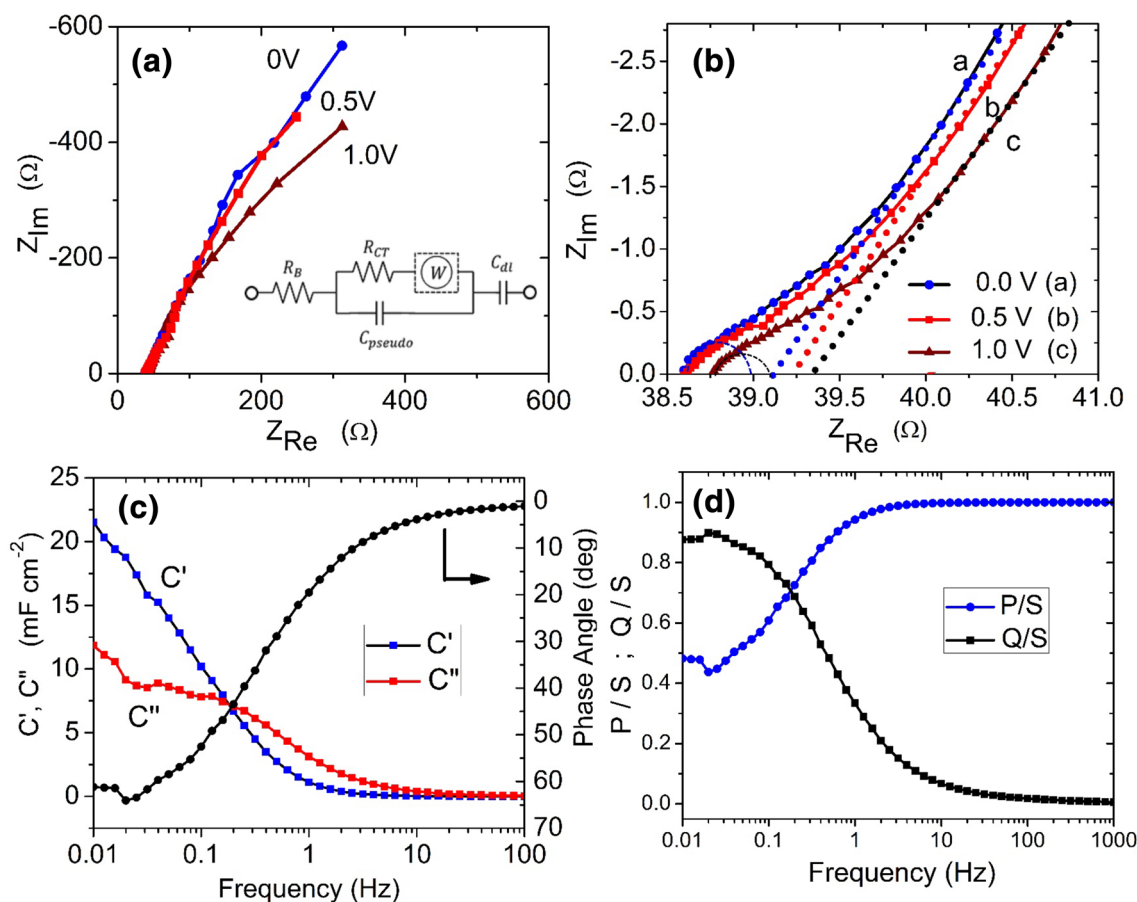


**Fig. 8** For PEDOT/ILG/graphene asymmetrical supercapacitor device HSC-O, **a** Nyquist plot with electrical equivalent circuit in the inset **b** expanded high and middle frequency Nyquist plot **c** frequency

dependence of phase angle, real, and imaginary capacitance  $C'$  and  $C''$  **d** frequency dependence of fraction of total reactive and active power

charge transfer resistance,  $R_{CT}$  and the Warburg impedance  $W$ . The expanded high and mid frequency region of the Nyquist plots which at frequencies  $> 1$  kHz reflects the bulk and between 500 and 10 Hz charge transfer resistance properties of the hybrid supercapacitor is shown in Fig. 8b. The effective internal resistance  $R_B$  contributed by the uncompensated electrolyte–electrode quantified by the real-axis high-frequency cut-off is given as 38.5, 38.6, and 38.8  $\Omega$  at 0, 0.5, and 1.0 V dc bias, respectively. The Nyquist plots in the high and middle frequency domain show broad arc-like features due the capacitance ( $C_{pseudo}$ ) in parallel with charge transfer resistance ( $R_{CT}$ ) originating from the resistance encountered by forwarding ion transfer processes at the electrode–electrolyte interface. The absence of the usual semicircle in the complex-plane plots in the high and middle frequency region is indicative of small charge transfer resistance. The broad arc was fitted as semicircle by simulation over a small frequency region of the impedance spectra based on the electrical equivalent circuit and Table 1 shows the simulation results. The mid frequency intercept of the semicircle shows a second cut-off at the real  $Z_{Re}$  axis which

**Table 1** Simulation results of the impedance spectra

DC bias (V)	$R_B$ ( $\Omega$ cm <sup>2</sup> )	$R_{CT}$ ( $\Omega$ cm <sup>2</sup> )	$R_\Omega$ ( $\Omega$ cm <sup>2</sup> )	$C$ (mF cm <sup>-2</sup> )
0	38.5	0.64	0.40	28.1
-0.5	38.6	0.64	0.46	35.9
-1	38.8	0.66	0.48	37.3

yields  $R_{CT}$  value of 0.64 and 0.66  $\Omega$  cm<sup>2</sup> at 0 and 1 V dc bias, respectively. The small  $R_{CT}$  values imply a favorable charge transport across the interface of ionic liquid electrolyte with PEDOT and graphene electrodes. The linear angularity at near 45° in the low-frequency region signifies the Warburg impedance ( $W$ ) which arises from the semi-infinite ion diffusive transport. The cut-off of the linear extension in this impedance region at the real  $Z_{Re}$  impedance axis gives a value  $R_S + R_\Omega$  where  $R_\Omega$  signifies 1/3rd of ionic resistances. The  $R_\Omega$  essentially arise from the resistance encountered by ions from distributed RC network of the pores in microporous PEDOT electrode.

As shown in Table 1, the  $R_{\Omega}$  values for hybrid supercapacitor at 0, 0.5, and 1 V dc bias are 0.4, 0.46, and  $0.48 \Omega \text{ cm}^2$ , respectively. It is apparent that most contribution to the internal resistance of the hybrid supercapacitor device arises from electrode contacts and to some extent from electrolyte which is mainly responsible for the limiting of specific power. The vertical increase in the imaginary impedance plot denotes the capacitive behavior of the supercapacitor which extends over a wide frequency domain beginning with the knee frequency at the end of the Warburg region. Table 1 shows the specific capacitance,  $C_{\text{SI}}$  of the supercapacitor device based on impedance at 0.01 Hz using,  $C_{\text{SI}} = (-2\pi f Z_{\text{Im}})^{-1}$  as 28.1, 35.9, and  $37.3 \text{ F cm}^{-2}$  at dc bias of 0, 0.5, and 1.0 V.

The rate capability and internal irreversible energy loss on power delivery of the hybrid supercapacitor HSC-O was carried out using Bode plot analysis. The measured specific capacitance of the hybrid supercapacitor,  $C_{\text{sc}}$  is characterized by a complex relation [61] involving the real capacitance,  $C'$  and imaginary capacitance,  $C''$

$$C_{\text{sc}}(\omega) = C'(\omega) - jC''(\omega). \quad (7)$$

The real capacitance  $C'$  is basically the effective capacitance component involved in the actual delivery of the stored capacitive energy to the load, and the irreversible dissipation of the stored energy within the system through various resistive or dielectric loss processes is represented by the imaginary capacitance  $C''$ . These are computed by the following equations [61],

$$C'(\omega) = \frac{-Z_{\text{Im}}(\omega)}{\omega|Z(\omega)|^2} \quad (8)$$

and

$$C''(\omega) = \frac{Z_{\text{Re}}(\omega)}{\omega|Z(\omega)|^2}. \quad (9)$$

The Bode plot in Fig. 8c shows the frequency dependence of  $C'$  and  $C''$ . The near  $0^\circ$  plateau response of  $C'$  over middle-to-high frequency indicates that the resistive response and the capacitive attributes of the hybrid device are evident from a rapid increase in  $C'(\omega)$  as the frequency decreases below 2.0 Hz. The nature of  $C'(\omega)$  in the low-frequency regime reflects on the properties of the electrode–electrolyte interface and the intrinsic electrochemical characteristics of each electrode of the hybrid supercapacitor cell. The increase in real capacitance over the practical frequency range of 0.01–1 Hz shows that both graphene and PEDOT film electrodes have reasonable access to the electrolyte ions. The still rising  $C'(\omega)$  at 0.01 Hz indicates that a complete charged state of the supercapacitor electrodes is yet to be reached. This is attributed to the diffusive ion transport usually seen in

porous electrodes. Figure 8c also shows the frequency dependence of the phase angle which at  $0^\circ$  in the high-frequency (resistive) regime rapidly increases to  $\sim 65^\circ$  at 0.01 Hz suggesting that the electrode–electrolyte interface has a favorable ion charge transfer situation for an enhanced capacitive action [62].

Bode plot of the imaginary capacitance  $C''(\omega)$  shown in Fig. 8c characterizes the resistive losses leading to irreversible dissipation of the stored energy. At a frequency  $f_m = 0.18 \text{ Hz}$ , one notices an onset of a slow variation of  $C''(\omega)$  with the frequency which is inferred to correspond to relaxation time  $\tau_r$  and provides a measure of the rate capability of the supercapacitor as it is normally associated with the swiftness of the capacitive discharge [60–62]. The high power density supercapacitors usually show low  $\tau_r = 1/f_m$  value which is  $\sim 5.5 \text{ s}$  in this case. In purely EDLC system, the  $C''(\omega)$  shows a peak corresponding to the relaxation time [61]. However, the supercapacitor cell investigated in this work is based on pseudo-capacitive and EDLC asymmetric electrodes, which may be a factor in not observing a definite peak in the  $C''(\omega)$  plot with the frequency [61]. This may lead to a lower value of the relaxation time than estimated from the onset of a gradient change in the  $C''(\omega)$  plot. The output power of the hybrid supercapacitor has both reactive  $Q$  and active  $P$  components given in a complex form,  $S(\omega) = P(\omega) + jQ(\omega)$ . This is because the supercapacitor acts as a capacitor at low and as a resistor at high frequencies. In the impedance analysis, both components of output power are related to the real  $C'$  and imaginary  $C''$  capacitances and complex power to the overall capacitance by the relations [61],

$$Q(\omega) = -\omega C'(\omega) |\Delta V_{\text{rms}}|^2 \quad (10)$$

$$P(\omega) = \omega C''(\omega) |\Delta V_{\text{rms}}|^2 \quad (11)$$

$$S(\omega) = -\omega C(\omega) |\Delta V_{\text{rms}}|^2. \quad (12)$$

Figure 8d presents, the frequency dependence of the fraction of the total reactive  $Q(\omega)/S(\omega)$  and active  $P(\omega)/S(\omega)$  power for the hybrid supercapacitor device. Close to 100% reactive power  $Q/S$  in the low-frequency range is observed when the capacitive storage property of the hybrid supercapacitor dominates. On the other hand, the active power  $P/S$  dissipated in the system decreases at lower frequency from a 100% value at the high frequencies. The cut-off between the two when  $Q = P$  is described as the transition from the capacitive to a resistive behavior of the supercapacitor device. The transitional frequency at 0.18 Hz is same as inferred from plateau in the  $C''$  plot shown in Fig. 8c. Based on the Eqs. (10–12), at transition,  $Q/S = P/S = 1/\sqrt{2}$

which corresponds to the phase angle of  $45^\circ$ . This measured phase angle of the hybrid supercapacitor device is close to  $45^\circ$  at the transition frequency of 0.18 Hz as shown in Fig. 8c.

### 3.7 PEDOT/ILG/graphene hybrid supercapacitor charging using solar cells

The PEDOT/ILG/graphene hybrid supercapacitor HSC-O with ionic liquid gel electrolyte is integrated with a silicon solar cell to demonstrate an energy-harvesting system. Integration of solar cells with the thin flexible solid-state supercapacitor energy storage has potential application in wearable electronics and similar portable low-power electronic devices. As shown schematically in Fig. 9a, in the solid-state design the supercapacitor is assembled in the thin flat format with overall thickness of  $< 1$  mm and therefore it can be easily mounted underneath the solar cell submodule without affecting the form factor. Figure 9b shows the electrical test circuit for evaluating the autonomous energy storage performance of the hybrid supercapacitor directly charged when solar cell submodule is exposed to light. A blocking diode prevents the hybrid supercapacitor from discharging into characteristic resistances  $R_S$  and  $R_{SH}$  of the solar cell under dark. The hybrid supercapacitor is charged when solar cell is exposed to white light of intensity  $\sim 70$  mW  $\text{cm}^{-2}$  which

is nearly the same intensity as that of the ambient outdoor light. The charging is initiated as switch S1 is closed and S2 is kept open. The energy storage performance of supercapacitor is evaluated by monitoring the voltage profile with time and the discharge profile is evaluated under open circuit and at various loads using computer controlled digital multimeter Agilent 34401A. Figure 9c shows the charging curves for cell voltage of 0.5 and 0.8 V, and discharge curves at various loads. The discharge profiles are obtained after light is turned off and S2 is closed. The discharge rate dependent on the load shows the discharge time of 200 s from peak stored voltage of 0.83–0.1 V at  $0.68$  A  $\text{g}^{-1}$  and 23 s at  $2.48$  A  $\text{g}^{-1}$ . For the cell charged to 0.5 V at charging current of  $0.35$  A  $\text{g}^{-1}$ , the corresponding times are 120, 90, and 20 s for discharge current of 0.21, 0.35, and  $1.55$  A  $\text{g}^{-1}$ , respectively. The charging profile of supercapacitor by solar cell is highly non-linear. Solar cell being a current source, supplies the short circuit current  $I_{SC} = I_L - I_D$  initially. The supercapacitor is charged quickly to 0.6 V within 25 s. As the supercapacitor voltage increases, the solar cell output characteristics shift to low current which slows the charging rate reaching 0.75 V in 54 s and full charging voltage of 0.83 V is obtained in 148 s. Figure 9d shows the charge retention characteristics of supercapacitor charged by solar cell to 0.8 and 0.5 V. The hybrid supercapacitor is charged rapidly to 0.70 V as the light over solar cell is turned-on. The

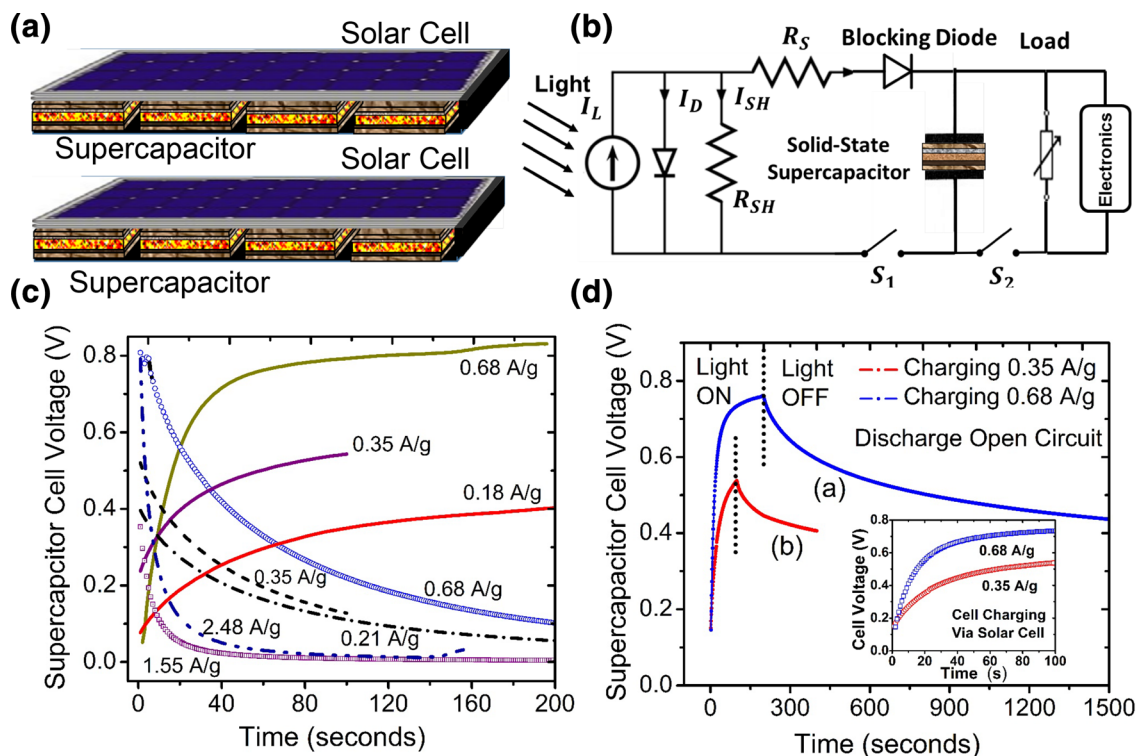


**Fig. 9** a Schematic of thin layer supercapacitor stacked with solar cell submodule. Characteristics of solar cell-integrated PEDOT/ILG/graphene hybrid supercapacitor device HSC-O, b electrical circuit for charging, c charge–discharge curves, d self-discharge curves

inset shows the expanded charging profile. The discharge curve is obtained under open circuit condition after the light incident on solar cell is turned off and S2 is kept open. The self-discharge characteristics show that for supercapacitor charged to 0.8 V, the voltage falls to 0.46 V over the monitored period of 1500 s (23 min) and for cell voltage of 5 V over 420 s (7 min). This extended energy storage period shows that the hybrid PEDOT/ILG/graphene supercapacitor holds considerable potential for self-powered electronics by storing solar electricity when integrated with solar cells. The drain current is about  $0.5 \text{ mA cm}^{-2}$ , which is considerably higher for most low-power portable electronics and at low current it can provide even extended powering times. The storage of solar electricity and power delivery characteristic of PEDOT/ILG/graphene hybrid supercapacitors appear quite promising for applications as autonomous energy source harvesting light energy for powering portable low-power and flexible electronics.

## 4 Conclusions

Hybrid supercapacitor using the electropolymerized PEDOT and graphene asymmetric electrodes were assembled with 1-butyl-3-methylimidazolium tetrafluoroborate ([BMIM][BF<sub>4</sub>]) ionic liquid gel. In the hybrid design, the energy storage is accomplished by storage of charges as the EDL capacitance at the graphene electrode and through the reversible faradic redox (doping and de-doping) process at the microporous PEDOT electrode while the increased operational potential of 2.7 V provided a boost to the energy density. Areal capacitance density  $> 102 \text{ mF cm}^{-2}$  is realized which is an improvement over the  $40 \text{ mF cm}^{-2}$  reported earlier for symmetrical graphene supercapacitors based on ionic liquid electrolytes. The PEDOT/ionic liquid gel/graphene hybrid supercapacitor cell shows specific capacitance of  $71 \text{ F g}^{-1}$  based on the CV data at low scan rates. By combining the micro-porosity of PEDOT, large  $600 \text{ m}^2 \text{ g}^{-1}$  surface area of graphene and high 2.7 V stability of conducting ([BMIM][BF<sub>4</sub>]) ionic liquid gel electrolyte, energy density of  $14.9 \text{ Wh kg}^{-1}$  at specific power rating of  $9.8 \text{ kW kg}^{-1}$  are realized, and stability over 2000 charge–discharge cycles is shown. Autonomous power storage application was demonstrated in an energy-harvesting circuit comprising silicon solar cell under ambient outdoor light. The storage of harvested solar electricity is realized by rapid  $< 100 \text{ s}$  charging of hybrid solid-state supercapacitor and it was shown that about 50% stored energy can be retained for over 1200 s, which is useful in powering portable low-power and flexible electronics.

**Acknowledgements** This research was supported by the National Science Foundation, under Award Number 1318202, “Partnership for Innovation in Electrochemical Energy Storage” which is gratefully acknowledged. The authors also acknowledge the Small Scale Integration and Packaging for funding support, ADLG-144, for use of Analytical and Diagnostics Laboratory (ADL) facilities.

## Compliance with ethical standards

**Conflict of interest** There are no conflicts to declare.

**Research involving human and animal participants** No involvement of human participants and/or animals in the research.

## References


1. Jost K, Stenger D, Perez CR, McDonough JK, Lian K, Gogotsi Y, Dion G (2013) Knitted and screen printed carbon-fiber supercapacitors for applications in wearable electronics. *Energy Environ Sci* 6:2698–2705
2. Hu L, Pasta M, Mantia FL, Cui L, Jeong S, Deshazer HD, Choi JW, Han SM, Cui Y (2010) Stretchable, porous, and conductive energy textiles. *Nano Lett* 10:708–714
3. Wang K, Zou W, Quan B, Yu A, Wu H, Jiang P, Wei Z (2011) An all-solid-state flexible micro-supercapacitor on a chip. *Adv Energy Mater* 1:1068–1072
4. Yan XB, Chen JT, Yang J, Xue QJ, Miele P (2010) Fabrication of free-standing, electrochemically active, and biocompatible graphene oxide-polyaniline and graphene-polyaniline hybrid papers. *ACS Appl Mater Interfaces* 2:2521–2529
5. Yuan L, Xiao X, Ding T, Zhong J, Zhang X, Shen Y, Hu B, Huang Y, Zhou J, Wang ZL (2012) Paper-based supercapacitors for self-powered nanosystems. *Angew Chem* 51:4934–4938
6. Zhang Z, Chen X, Chen P, Guan G, Qiu L, Lin H, Yang Z, Bai W, Luo Y, Peng H (2014) Integrated polymer solar cell and electrochemical supercapacitor in a flexible and stable fiber format. *Adv Mater* 26:466–470
7. Murakami T, Kawashima N, Miyasaka T (2005) A high-voltage dye-sensitized photocapacitor of a three-electrode system. *Chem Commun* 26:3346–3348
8. Zhan Y, Mei Y, Zheng L (2014) Materials capability and device performance in flexible electronics for the internet of things. *J Mater Chem C* 2:1220–12324
9. Somov A, Ho C, Passerone R, Evans J, Wright P (2012) Towards extending sensor node lifetime with printed supercapacitors, wireless sensor networks. *Proc 9th European conference (EWSN 2012)*. Trento, pp 212–227
10. Kotz R, Carlen M (2000) Principles and applications of electrochemical capacitors. *Electrochim Acta* 45:2483–2498
11. Zhang LL, Zhao XS (2009) Carbon-based materials as supercapacitor electrodes. *Chem Soc Rev* 38:2520–2531
12. Candelaria SL, Shao Y, Zhou W, Li X, Xiao J, Zhang JG, Wang Y, Liu J, Li J, Cao G (2012) Nanostructured carbon for energy storage and conversion. *Nano Energy* 1:195–220
13. Wang G, Zhang L, Zhang J (2012) A review of electrode materials for electrochemical supercapacitors. *Chem Soc Rev* 41:797–828
14. Snook G, Kao P, Best A (2011) Conducting-polymer-based supercapacitor devices and electrodes. *J Power Sources* 196:1–12
15. Wang K, Wu H, Meng Y, Wei Z (2014) Conducting polymer nanowire arrays for high performance supercapacitors. *Small* 10:14–31



16. Liu R, Duay J, Lee SB (2011) Heterogeneous nanostructured electrode materials for electrochemical energy storage. *Chem Commun* 47:1384–1404
17. Khomenko V, Raymundo-Piñero E, Frackowiak E, Béguin F (2006) High-voltage asymmetric supercapacitors operating in aqueous electrolyte. *Appl Phys A* 82:567–573
18. Wu ZS, Ren W, Wang DW, Li F, Liu B, Cheng HM (2010) High-energy MnO<sub>2</sub> nanowire/graphene and graphene asymmetric electrochemical capacitors. *ACS Nano* 4:5835–5842
19. Tang Z, Tang C, Gong H (2012) A high energy density asymmetric supercapacitor from nanoarchitected Ni(OH)<sub>2</sub>/carbon nanotube electrodes. *Adv Funct Mater* 22:1272–1278
20. Fan Z, Yan J, Wei T, Zhi L, Ning G, Li T, Wei F (2011) Asymmetric supercapacitors based on graphene/MnO<sub>2</sub> and activated carbon nanofiber electrodes with high power and energy density. *Adv Funct Mater* 21:2366–2375
21. Wang R, Yan X (2014) Superior asymmetric supercapacitor based on Ni–Co oxide nanosheets and carbon nanorods. *Sci Rep* 4:3712
22. Wang X, Yan C, Sumboja A, Lee PS (2014) High performance porous nickel cobalt oxide nanowires for asymmetric supercapacitor. *Nano Energy* 3:119–126
23. Shao Y, Wang H, Zhang Q, Li Y (2013) High-performance flexible asymmetric supercapacitors based on 3D porous graphene/MnO<sub>2</sub> nanorod and graphene/Ag hybrid thin-film electrodes. *J Mater Chem C* 1:1245–1251
24. Villers D, Jobin D, Soucy C, Cossement D, Chahine R, Breau L, Bélanger D (2003) Influence of the range of electroactivity and capacitance of conducting polymers on the performance of carbon conducting polymer hybrid supercapacitor. *J Electrochem Soc* 150:A747–A752
25. Park JH, Park OO (2002) Hybrid electrochemical capacitors based on polyaniline and activated carbon electrodes. *J Power Sources* 111:185–190
26. Sidhu NK, Rastogi AC (2016) Electrochemical performance of supercapacitors based on carbon nanofoam composite and microporous poly(3, 4-ethylenedioxythiophene) thin film asymmetric electrodes. *Mater Chem Phys* 176:75–86
27. Meng FH, Ding Y (2011) Sub-micrometer-thick all-solid-state supercapacitors with high power and energy densities. *Adv Mater* 23:4098–4102
28. Meng C, Liu C, Chen L, Hu C, Fan S (2010) Highly flexible and all-solid-state paper-like polymer supercapacitors. *Nano Lett* 10:4025
29. Lin H, Li L, Ren J, Cai Z, Qiu L, Yang Z, Peng H (2013) Conducting polymer composite film incorporated with aligned carbon nanotubes for transparent, flexible and efficient supercapacitor. *Sci Rep* 3:1353. <https://doi.org/10.1038/srep01353>
30. Hu S, Rajamani R, Yu X (2012) Flexible solid-state paper based carbon nanotube supercapacitor. *Appl Phys Lett* 100:104103. <https://doi.org/10.1063/1.3691948>
31. Lehtimäki S, Suominen M, Damlin P, Tuukkanen S, Kvarnström C, Lupo D (2015) Preparation of supercapacitors on flexible substrates with electrodeposited PEDOT/graphene composites. *ACS Appl Mater Interfaces* 7:22137–22147
32. He Y, Chen W, Gao C, Zhao J, Li Z, Xie E (2013) An overview of carbon materials for flexible electrochemical capacitors. *Nanoscale* 5:8799–8820
33. Qiying L, Wang S, Sun H, Luo J, Xiao J, Xiao JW, Xiao F, Wang S (2016) Solid-state thin-film supercapacitors with ultrafast charge/discharge based on N-doped-carbon-tubes/Au-nanoparticles-doped-MnO<sub>2</sub> nanocomposites. *Nano Lett* 16:40–47
34. Gao H, Xiao F, Ching CB, Duan H (2012) Flexible all-solid-state asymmetric supercapacitors based on free-standing carbon nanotube/graphene and Mn<sub>3</sub>O<sub>4</sub> nanoparticle/graphene paper electrodes. *ACS Appl Mater Interfaces* 4:7020–7026
35. Choi B, Chang S, Kang H, Park C, Kim H, Hong W, Lee S, Huh Y (2012) High performance of a solid-state flexible asymmetric supercapacitor based on graphene films. *Nanoscale* 4:4983–4988
36. Xiao X, Ding T, Yuan L, Shen Y, Zong Q, Zhang X, Cao Y, Hu B, Zhai T, Gong L, Chen J, Tong Y, Zhou J, Wang Z (2012) WO<sub>3-x</sub>/MoO<sub>3-x</sub> core/shell nanowires on carbon fabric as an anode for all-solid-state asymmetric supercapacitors. *ACS Nano* 2:1328–1332
37. Kurra N, Wang R, Alshareef HN (2015) All conducting polymer electrodes for asymmetric solid-state supercapacitors. *J Mater Chem A* 3:7368–7374
38. Zhang S, Sun N, He X, Lu X, Zhang X (2006) Physical properties of ionic liquids database and evaluation. *J Phys Chem Ref Data* 35:1475–1517
39. Kang YJ, Chun DJ, Lee SS, Kim BY, Kim JH, Chung H, Lee SY, Kim W (2012) All-solid-state flexible supercapacitors fabricated with bacterial nanocellulose papers, carbon nanotubes and triblock-copolymer ion gels. *ACS Nano* 6:6400–6406
40. Pandey GP, Rastogi AC, Westgate CR (2013) Polyacrylonitrile and 1-ethyl-3-methylimidazolium thiocyanate based gel polymer electrolyte for solid-state supercapacitors with graphene electrodes. *ECS Trans* 50:145–151
41. Pandey GP, Rastogi AC, Westgate CR (2014) All-solid-state supercapacitors with poly(3, 4-ethylenedioxythiophene)-coated carbon fiber paper electrodes and ionic liquid gel polymer electrolyte. *J Power Sources* 245:857–864
42. Pandey GP, Rastogi AC (2012) Solid-state supercapacitors based on pulse polymerized poly(3, 4-ethylenedioxythiophene) electrodes and ionic liquid gel polymer electrolyte. *J Electrochem Soc* 159:A1664–A1671
43. Groenendaal L, Jonas F, Freitag D, Pielartzik H, Reynolds JR (2000) Poly(3,4-ethylenedioxythiophene) and its derivatives: past, present, and future. *Adv Mater* 12:481–494
44. Pandey GP, Rastogi AC (2013) Synthesis and characterization of pulsed polymerized poly(3, 4-ethylenedioxythiophene) electrodes for high-performance electrochemical capacitors. *Electrochim Acta* 87:158–168
45. Österholm AM, Shen DE, Dyer AL, Reynolds JR (2013) Optimization of PEDOT films in ionic liquid supercapacitors: demonstration as a power source for polymer electrochromic devices. *ACS Appl Mater Interfaces* 5:13432–13440
46. Wee G, Salim T, Lam Y, Mhaisalkar SG, Srinivasan M (2011) Printable photo-supercapacitor using single-walled carbon nanotubes. *Energy Environ Sci* 4:413–416
47. Sharma RK, Rastogi AC, Desu SB (2008) Manganese oxide embedded polypyrrole nanocomposites for electrochemical supercapacitor. *Electrochem Commun* 10:268–272
48. Garreau S, Louarn G, Buisson JP, Froyer G, Lefrant S (1999) In situ spectroelectrochemical raman studies of poly(3,4-ethylenedioxythiophene) (PEDT). *Macromolecules* 32:6807–6812
49. Pfluger P, Street GB (1984) Chemical, electronic, and structural properties of conducting heterocyclic polymers: a view by XPS. *J Chem Phys* 80:544–553
50. Han DH, Kim JW, Park SM (2006) Electrochemistry of conductive polymers 38. Electrodeposited poly(3,4-ethylenedioxythiophene) studied by current sensing atomic force microscopy. *J Phys Chem B* 110:14874–14880
51. James DW, Mayers RE (1982) Ion-ion-solvent interactions in solution. I. Solutions of LiClO<sub>4</sub> in acetone. *Aust J Chem* 35:1775–1784
52. Gupta A, Chen G, Joshi P, Tadigadapa S, Eklund PC (2006) Raman Scattering from High-Frequency Phonons in Supported n-Graphene Layer Films. *Nano Lett* 6:2667–2673
53. Childres I, Jaureguib LA, Park W, Cao H., Chen YP (2013) Raman spectroscopy of graphene and related material. In: Jang JI (ed)

- New developments in photon & materials research. Nova Science, Hauppauge
54. Saito R, Hofmann M, Dresselhaus G, Jorio A, Dresselhaus MS (2011) Raman spectroscopy of graphene and carbon nanotubes. *Adv Phys* 30:413–550
  55. Gao H, Xiao F, Ching CB, Duan H (2012) High-performance asymmetric supercapacitor based on graphene hydrogel and nanostructured MnO<sub>2</sub>. *ACS Appl Mater Interfaces* 4:2801–2810
  56. Shen J, Yang C, Li X, Wang G (2013) High-performance asymmetric supercapacitor based on nanoarchitected polyaniline/graphene/carbon nanotube and activated graphene electrodes. *ACS Appl Mater Interfaces* 5:8467–8476
  57. Lu X, Yu M, Wang G, Tong Y, Li Y (2014) Flexible solid-state supercapacitors: design, fabrication and applications. *Energy Environ Sci* 7:2160–2181
  58. Duay J, Gillette E, Liu R, Lee SB (2012) Highly flexible pseudocapacitor based on freestanding heterogeneous MnO<sub>2</sub>/conductive polymer nanowire arrays. *Phys Chem Chem Phys* 14:3329–3337
  59. Jin Y, Chen HY, Chen MH, Liu N, Li QW (2013) Graphene-patched CNT/MnO<sub>2</sub> nanocomposite papers for the electrode of high-performance flexible asymmetric supercapacitors. *ACS Appl Mater Interfaces* 5:3408–3416
  60. Choi BG, Chang SJ, Kang HW, Park CP, Kim HJ, Hong WH, Lee S, Huh YS (2012) High performance of a solid-state flexible asymmetric supercapacitor based on graphene films. *Nanoscale* 4:4983–4988
  61. Taberna PL, Simon JF (2003) Electrochemical characteristics and impedance spectroscopy studies of carbon-carbon supercapacitors. *J Electrochem Soc* 150:A292–A300
  62. Sheng K, Sun Y, Li C, Yuan W, Shi G (2012) Ultrahigh-rate supercapacitors based on electrochemically reduced graphene oxide for ac line-filtering. *Sci Rep* 2:247–252

## Affiliations

Amr M. Obeidat<sup>1,2</sup> · A. C. Rastogi<sup>1</sup> 

✉ A. C. Rastogi  
arastogi@binghamton.edu

<sup>2</sup> Electrical Engineering Department, The Hashemite University, Zarqa 13115, Jordan

<sup>1</sup> Department of Electrical & Computer Engineering, Center for Autonomous Solar Power, CASP Binghamton University, State University of New York, Binghamton, NY 13902, USA